

Sensitivity analysis for small imaging domains using the frequency-domain transport equation

Xuejun Gu^a, Kui Ren^b and Andreas H. Hielscher^{a, c}

^aDepartment of Biomedical Engineering, Columbia University, NY 10027;

^bDepartment of Applied Physics and Applied Mathematics, Columbia University, NY 10027;

^cDepartment of Radiology, Columbia University, NY 10027

ABSTRACT

Optical tomography of small tissue volumes, as they are encountered in rodent or finger imaging, holds great promise as the signal-to-noise levels are usually high and the spatial resolutions are much better than that of large imaging domains. To accurately model the light propagation in these small domains, radiative transport equations have to be solved directly. In the study at hand, we use the frequency-domain equation of radiative transfer (ERT) to perform a sensitivity study. We determine optimal source-modulation frequencies for which variations in optical properties, size, and location of a tissue inhomogeneity lead to maximal changes in the amplitude and phase of the measured signal. These results will be useful in designed experiments and optical tomographic imaging system.

Keywords: Optical tomography, equation of radiative transfer, finite volume method, signal-to-noise

1. INTRODUCTION

Recent years have seen an increased interest in optically imaging of small tissue volumes. This interest is mainly driven by advances in small animal models of diseases and the need to monitor disease progression and the influence of various drugs on treatment outcome. Optical tomographic imaging of small tissue volumes faces particular challenges since the diffusion approximation, which is typically used to model light propagation in larger tissue structures, becomes less accurate and often fails in this case. More complex models of light propagation, such as provided by the equation of radiative transfer (ERT) have to be applied. Only a limited number of groups have attempted to solve the ERT for problems encountered in optical tomography, because implementing an efficient and accurate ERT algorithm is considerably more challenging than using the diffusion equation. Works include solutions to the two-dimensional time-dependent and time-independent ERT^{1,2} and the three-dimensional time-independent ERT.³⁻⁶ Recently, our group has introduced the first frequency-domain ERT code that can be used for optical tomographic imaging.^{7,8}

In the study at hand, we use the frequency-domain ERT code to investigate the detection limits of tissue inhomogeneities with varying optical properties, sizes, and locations. Similar studies have been performed before but did not focus on small tissue volumes and neither used the ERT as a light-propagation model. For example, Boas et al⁹ studied the effect of the source-modulation frequency on the quantification and localization accuracy of scattering and absorbing perturbation in a 60-mm thick infinite slab, which mimicked light propagation in female breast tissue. Their analysis was based on analytical solution for the frequency-domain diffusion equation. Toronov et al¹⁰ analyzed the signal-sensitivity-to-noise ratio of phase measurement at different modulation frequencies using Monte-Carlo simulation of light propagation in the human head. Sensitivity studies for fluorescence tomography were presented by Fedele et al.¹¹ By performing sensitivity studies particular for small tissue geometries using the frequency ERT, our work provides an important insight into the potentials and limitations of small tissue tomography and will help in the design of appropriate experimental setups and tomographic instrumentation.

Further author information:

X. G: E-mail: xg2108@columbia.edu, Telephone: 1 212 854 5885

A.H.H: E-mail: ahh2004@columbia.edu, Telephone: 1 212 854 5080

Diffuse Optical Imaging of Tissue, edited by Brian W. Pogue, Rinaldo Cubeddu,
Proc. of SPIE-OSA Biomedical Optics, SPIE Vol. 6629, 66291Q, © 2007 SPIE-OSA · 1605-7422/07/\$18

The paper is organized as follows: in Section 2, we will provide some theoretical and experimental background for our analysis and define the terms signal-to-noise ratio (SNR) and signal-sensitivity-to-noise ratio (SSNR). In Section 3 we will present our numerical analysis, which is followed by a discussion of the results.

2. SIGNAL AND NOISE MODEL

2.1. Theoretical background of signal and signal sensitivity based on ERT

The frequency-domain equation of radiative transfer that describes the photon density in the phase space, i.e., as a function of position $\mathbf{x} \in \mathcal{D} \subset \mathbb{R}^n$ and direction $\boldsymbol{\theta} \in S^{n-1}$ (unit sphere of \mathbb{R}^n) is given by:⁷

$$\begin{aligned} \left(-\frac{i\omega}{v} + \boldsymbol{\theta} \cdot \nabla + \mu_t(\mathbf{x})\right) \psi(\mathbf{x}, \boldsymbol{\theta}) - \mu_s(\mathbf{x}) \int_{S^{n-1}} k(\boldsymbol{\theta} \cdot \boldsymbol{\theta}') \psi(\mathbf{x}, \boldsymbol{\theta}') d\boldsymbol{\theta}' &= 0 && \text{in } \mathcal{D} \times S^{n-1} \\ \psi(\mathbf{x}, \boldsymbol{\theta}) &= q(\mathbf{x}, \boldsymbol{\theta}) && \text{on } \Gamma_-. \end{aligned} \quad (1)$$

Here $i = \sqrt{-1}$, v is the speed of light in the medium, and ω is the source modulation frequency. The parameter $\mu_t = \mu_a + \mu_s$, with μ_a and μ_s being the absorption and scattering coefficient, respectively. $\psi(\mathbf{x}, \boldsymbol{\theta})$ is the radiance at position \mathbf{x} ($\mathbf{x} \in \mathcal{D}$) travelling in direction $\boldsymbol{\theta}$ with the unit of $Wm^{-2}sr^{-1}$, here note that $\psi(\mathbf{x}, \boldsymbol{\theta})$ is the frequency dependent. $q(\mathbf{x}, \boldsymbol{\theta})$ is source with the unit of $Wm^{-3}sr^{-1}$ defined on the boundary set: $\Gamma_{\pm} = \{(\mathbf{x}, \boldsymbol{\theta}) \in \partial\mathcal{D} \times S^{n-1} \text{ s.t. } \pm\boldsymbol{\theta} \cdot \boldsymbol{\nu}(\mathbf{x})\}$. with $\boldsymbol{\nu}(\mathbf{x})$ the outward unit normal to the domain at $\mathbf{x} \in \partial\mathcal{D}$. The ‘‘collision’’ kernel $k(\boldsymbol{\theta} \cdot \boldsymbol{\theta}')$, which describes the probability that photons traveling in direction $\boldsymbol{\theta}'$ scatter into direction $\boldsymbol{\theta}$, is a positive function independent of \mathbf{x} and satisfies the normalization condition: $\int_{S^{n-1}} k(\boldsymbol{\theta} \cdot \boldsymbol{\theta}') d\boldsymbol{\theta}' = 1$. The scattering kernel for light propagation in tissues is chosen here as the Henyey-Greenstein phase function.^{12,13}

Solving equation (1) results in a value for the radiance ψ . In the optical tomography experiments, however, one typically measures the outgoing flux, which is given by:

$$J(\mathbf{x}_d) = \int_{\Gamma_+} \boldsymbol{\theta}_d \cdot \boldsymbol{\nu}(\mathbf{x}_d) \psi(\mathbf{x}_d, \boldsymbol{\theta}_d) d\boldsymbol{\theta}_d. \quad (2)$$

Here \mathbf{x}_d is the position of detector and $J(\mathbf{x}_d)$ is a complex functional of the optical parameters μ_a and μ_s .

If we denote $(\delta\mu_a, \delta\mu_s)$ the perturbation of (μ_a, μ_s) , we can define the signal sensitivity as

$$\delta J(\mathbf{x}_d)(\delta\mu_a, \delta\mu_s) = \int_{\Gamma_+} \boldsymbol{\theta}_d \cdot \boldsymbol{\nu}(\mathbf{x}_d) \delta\psi(\mathbf{x}_d, \boldsymbol{\theta}_d) d\boldsymbol{\theta}_d. \quad (3)$$

After a perturbation over the transport solution, we obtain the following transport equation for $\delta\psi$

$$\begin{aligned} \left(-\frac{i\omega}{v} + \boldsymbol{\theta} \cdot \nabla + \mu_t(\mathbf{x})\right) \delta\psi(\mathbf{x}, \boldsymbol{\theta}) &= \mu_s(\mathbf{x}) \int_{S^{n-1}} k(\boldsymbol{\theta} \cdot \boldsymbol{\theta}') \delta\psi(\mathbf{x}, \boldsymbol{\theta}') d\boldsymbol{\theta}' \\ &- \left(\delta\mu_a(\mathbf{x}) + \delta\mu_s(\mathbf{x})\right) \psi(\mathbf{x}, \boldsymbol{\theta}) + \delta\mu_s(\mathbf{x}) \int_{S^{n-1}} k(\boldsymbol{\theta} \cdot \boldsymbol{\theta}') \psi(\mathbf{x}, \boldsymbol{\theta}') d\boldsymbol{\theta}' \end{aligned} \quad (4)$$

with boundary condition:

$$\delta\psi(\mathbf{x}, \boldsymbol{\theta}) = 0 \quad \text{on } \Gamma_-. \quad (5)$$

We now introduce the adjoint transport Green’s function $G(\mathbf{x}, \boldsymbol{\theta})$, which solves the following transport equation:

$$\left(-\frac{i\omega}{v} - \boldsymbol{\theta} \cdot \nabla + \mu_t(\mathbf{x})\right) G(\mathbf{x}, \boldsymbol{\theta}; \mathbf{x}_d, \boldsymbol{\theta}_d) = \mu_s(\mathbf{x}) \int_{S^{n-1}} k(\boldsymbol{\theta} \cdot \boldsymbol{\theta}') G(\mathbf{x}, \boldsymbol{\theta}; \mathbf{x}_d, \boldsymbol{\theta}_d) d\boldsymbol{\theta}' \quad (6)$$

with boundary condition:

$$G(\mathbf{x}, \boldsymbol{\theta}; \mathbf{x}_d, \boldsymbol{\theta}_d) = \delta(\boldsymbol{\theta} - \boldsymbol{\theta}_d) \delta(\mathbf{x} - \mathbf{x}_d) \quad \text{on } \Gamma_+. \quad (7)$$

If we multiply (4) by $G(\mathbf{x}, \boldsymbol{\theta}; \mathbf{x}_d, \boldsymbol{\theta}_d)$, multiply (6) by $\delta\psi$, and use integration by parts over the two equation, we obtain:

$$\delta\psi(\mathbf{x}_d, \boldsymbol{\theta}_d) = \int_X G(\mathbf{x}, \boldsymbol{\theta}; \mathbf{x}_d, \boldsymbol{\theta}_d) \left(-\left(\delta\mu_a(\mathbf{x}) + \delta\mu_s(\mathbf{x})\right) \psi(\mathbf{x}, \boldsymbol{\theta}) + \delta\mu_s(\mathbf{x}) \int_{S^{n-1}} k(\boldsymbol{\theta} \cdot \boldsymbol{\theta}') \psi(\mathbf{x}, \boldsymbol{\theta}') d\boldsymbol{\theta}' \right) d\mathbf{x} d\boldsymbol{\theta}. \quad (8)$$

where $X = \mathcal{D} \times S^{n-1}$. This tells us that the signal sensitivity is given by

$$\delta J(\mathbf{x}_d)(\delta\mu_a, \delta\mu_s) = \int_{\mathcal{D}} \left(\Phi_a \delta\mu_a(\mathbf{x}) + \Phi_s \delta\mu_s(\mathbf{x}) \right) d\mathbf{x}, \quad (9)$$

with

$$\Phi_a = - \int_{\Gamma_+} \boldsymbol{\theta}_d \cdot \boldsymbol{\nu} \int_{S^{n-1}} G(\mathbf{x}, \boldsymbol{\theta}; \mathbf{x}_d, \boldsymbol{\theta}_d) \psi(\mathbf{x}, \boldsymbol{\theta}) d\boldsymbol{\theta} d\boldsymbol{\theta}_d; \quad (10)$$

and

$$\Phi_s = - \int_{\Gamma_+} \boldsymbol{\theta}_d \cdot \boldsymbol{\nu} \int_{S^{n-1}} G(\mathbf{x}, \boldsymbol{\theta}; \mathbf{x}_d, \boldsymbol{\theta}_d) \left(\psi(\mathbf{x}, \boldsymbol{\theta}) - \int_{S^{n-1}} k(\boldsymbol{\theta} \cdot \boldsymbol{\theta}') \psi(\mathbf{x}, \boldsymbol{\theta}') d\boldsymbol{\theta}' \right) d\boldsymbol{\theta} d\boldsymbol{\theta}_d. \quad (11)$$

Φ_a and Φ_s are absorption and scattering sensitivity functions, respectively.¹ In this paper we are interested in the dependencies of those functions on the source-modulation frequency, and the location, diameter, and contrast of an optical inhomogeneity.

A look at the above asymptotics tells us that the signal sensitivity (δJ) in measured data include contributions from the perturbation of absorption and of scattering. In the frequency-domain, δJ is a complex function, which includes a real part and an imaginary part. This provides a possibility for separating the absorption from scattering effects in our reconstruction process. The condition for such a separation is that the functions that form the real and imaginary parts of the coefficient matrix make this matrix diagonally dominant. Although we do not present a rigorous mathematical proof, the above argument is supported by a similar existing theory on the simultaneous reconstruction of the two parameters based on diffusion theory.¹⁴ Furthermore, because the signal sensitivity can be separated into the perturbation of the absorption coefficient $\delta\mu_a$ and scattering coefficient $\delta\mu_s$ (see Eq. (9)) we can discuss the SSNR for absorption and scattering perturbations, respectively.

2.2. Experimental background of signal, signal sensitivity, and noise

With fiber-based optical experimental measurement, the flux $J(\mathbf{x}_d)$ (signal measured) is the summary of radiance's component on the boundary normal direction. In the frequency domain measurement, the signal, consisting of amplitude (AC) and phase delay (ϕ), can be explicitly written as:

$$J(\mathbf{x}_d)(\mu_a, \mu_s) = AC e^{i\phi}. \quad (12)$$

Here A and ϕ refers to measured amplitude and phase. Consequently, the signal sensitivity $\delta J(\mathbf{x}_d)$ defined as the signal caused by optical properties perturbation is

$$\delta J(\mathbf{x}_d)(\delta\mu_a, \delta\mu_s) = AC^t e^{i\phi^t} - AC^h e^{i\phi^h}. \quad (13)$$

where AC^t, ϕ^t are the amplitude and phase with perturbation and AC^h, ϕ^h without perturbation. Considering that the physically measured signals are denoted as amplitude and phase we define the signal amplitude sensitivity (δAC) and signal phase sensitivity ($\delta\phi$) as $\delta AC = AC^t - AC^h$ and $\delta\phi = \phi^t - \phi^h$, respectively. All measured signals contain some form of noise. In optical tomographic imaging systems, certain types of noise, such as that originating from inaccurate positioning of detectors and sources, can be eliminated by careful calibration. Others noise forms, such as Johnson noise or shot noise, which are intrinsic phenomena in all electronic circuits, are impossible to avoid. Theoretical and experimental analysis of these noise models and how they effect optical measurement systems have been given by Toronov et al¹⁰ and Tao et al.¹⁵ When one considers small imaging domains, the optical signals are usually relatively strong and thus shot noise is the dominant noise sources. This allows us, in this study, to rely on the analysis provided by Toronov et al, who derived the following expressions for the noises (standard deviations of signal fluctuation) in the DC intensity (σ_{DC}), AC amplitudes (σ_{AC}), and phase (σ_ϕ) measurements:

$$\sigma_{DC} \propto \sqrt{\langle DC \rangle}; \quad (14)$$

$$\sigma_{AC} \propto \sqrt{\langle DC \rangle}; \quad (15)$$

$$\sigma_\phi \propto \frac{1}{\langle AC \rangle} \propto \frac{\langle AC \rangle}{\sqrt{\langle DC \rangle}}, \quad (16)$$

where DC, AC, and ϕ is the DC intensity, AC amplitude, and phase measurements respectively in the experiment. The " $\langle \rangle$ " denotes an ensemble measurement average.

2.3. Signal-to-noise ratio (SNR) and signal-sensitivity-to-noise ratio (SSNR)

With the above signal and noise models in place, we can define the term signal-to-noise ratio (SNR) for the AC amplitude and phase as follows:

$$SNR_{AC}(\omega) = \frac{\langle AC \rangle}{\sigma_{AC}} \propto \frac{\langle AC \rangle}{\sqrt{\langle DC \rangle}}; \quad (17)$$

$$SNR_{\phi}(\omega) = \frac{\langle \phi \rangle}{\sigma_{\phi}} \propto \frac{\langle \phi \rangle}{\frac{\sigma_{AC}}{\langle AC \rangle}} \propto \langle \phi \rangle \cdot SNR_{AC}. \quad (18)$$

Therefore the SNR is the ratio of the signal divided by the noise in the measurements, given by the standard deviation σ . The value of the SNR is important if one wants to determine the quality of a signal available for a given tissue geometry and composition. If we want to determine whether a heterogeneity is detectable, we need to look at the effect this heterogeneity has on the measurements. Therefore, we define here the term signal-sensitivity-to-noise ratio (SSNR) for the AC amplitude ($SSNR_{AC}$) and phase ($SSNR_{\phi}$) as follows:

$$SSNR_{AC}(\omega) = \frac{\langle \delta AC \rangle}{\sigma_{AC}} \quad (19)$$

$$SSNR_{\phi}(\omega) = \frac{\langle \delta \phi \rangle}{\sigma_{\phi}} \propto (\langle \phi^t \rangle - \langle \phi^h \rangle) \cdot SNR_{AC}. \quad (20)$$

Here, the SSNR is the ratio of the signal sensitivity (AC sensitivity δAC or phase sensitivity $\delta \phi$) divided by the noise in the measurement. Note that both SNR and SSNR are frequency dependent, as AC amplitude and phase are frequency dependent.

3. NUMERICAL FREQUENCY SENSITIVITY ANALYSIS

Fig.1 illustrates the general tissue geometry used throughout this work. The computational domain is defined by $D := \{(x, y, z)^T \mid x^2 + y^2 \leq 1; 0 \leq z \leq 2\}$. In the simulations, we place a point source on $\mathbf{x}_s = (1, 0, 1)^T$. Detectors are evenly distributed on a circle defined by $\Gamma := \{(x, y, z)^T \mid x^2 + y^2 = 1; z = 1\}$. We refer to specific detectors by numbering them counter-clockwise from 1 through 12 starting at the source position S. The domain is discretized into approximately 17000 tetrahedral elements and 48 directions (s6 - with full level symmetry). A cylindrical heterogeneity with varying diameter and optical properties is placed at various distances off center. Detailed analysis can be found in.¹⁶

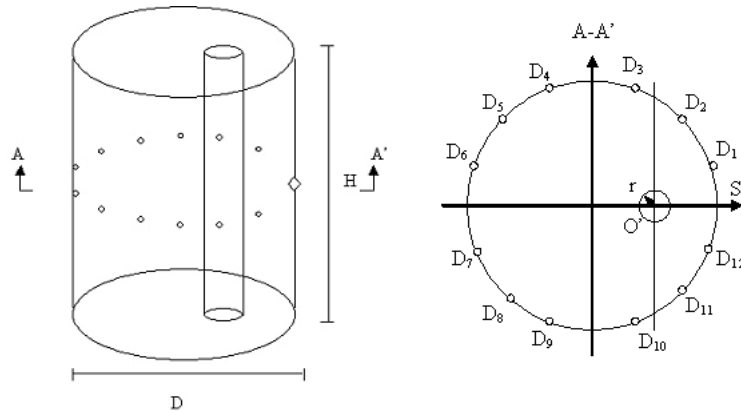


Figure 1. Geometric setup for numerical simulation, the diameter of the cylinder $D = 2$ cm, and height $H = 2$ cm. Sources are identified by diamonds and detectors by circles.

3.1. SSNR studies with absorbing perturbations

We start by examining the effects of absorption perturbations. In these cases, only the absorption property of the heterogeneity is varied. The scattering properties of the heterogeneity are identical to that of the background medium. The signal's amplitude sensitivity (δAC) and phase sensitivity ($\delta\phi$) are determined as a function of different absorption coefficients, sizes, and locations of the heterogeneity. We vary the source-modulation frequency and show SSNR curves for the different detector locations. A summary of all cases studied are listed in Table 1.

Table 1. Summary of different cases used for the sensitivity analysis with absorption perturbations

	Testing Cases*	$\mu_a (cm^{-1})$	$\mu_s (cm^{-1})$	r (cm)	$OO' (cm)$
	Reference case	0.1	10.0	0.25	0.5
	$2.0\mu_a, r = 0.25cm, OO' = 0.50cm$				
Strength	$1.2\mu_a$	0.06	10.0	0.25	0.5
	$1.5\mu_a$	0.075	10.0	0.25	0.5
Size	$r = 0.15cm$	0.1	10.0	0.15	0.5
	$r = 0.35cm$	0.1	10.0	0.35	0.5
Location	$OO' = 0.0cm$	0.1	10.0	0.25	0.0
	$OO' = 0.25cm$	0.1	10.0	0.25	0.25

In Figures 2(a) and 2(b), δAC and $\delta\phi$ at different detector position as a function of the modulation frequencies are plotted for the reference case (see Table 2). Here, δAC decrease as the modulation frequency increases or as the distance between a detector and sources pair increases. $\delta\phi$ show a reverse dependency. They increases as frequency or source-detector distances increases.

Figures 2(c) and 2(d) show the normalized SSNRs for the reference case at different detector positions as a function of the modulation frequency. Again, all these SSNR curves are normalized to the 100MHz point. Increasing the modulation frequency leads to a decrease in the $SSNR_{AC}$ (see Fig. 2(c)). This is in accordance with Eq. (19) because the signal's amplitude sensitivity (δAC) decreases with modulation frequency and at the same time the AC amplitude noise (σ_{AC}) is constant. Rather than showing a steady decrease, the $SSNR_{\phi}$ reaches a distinct maximum at 400MHz for all detector positions. That a maximum occurs in the SSNR for the phase can be understood by looking at Eq. (20). The $SSNR_{\phi}$ is proportional to the ratio of the signal's phase sensitivity ($\delta\phi$) and the phase noise (σ_{ϕ}). As the modulation frequency increases, both $\delta\phi$ and (σ_{ϕ}) are increasing leading to some characteristic maximum in these $SSNR_{\phi}$ curves.

3.1.1. Absorption perturbation strength

To investigate how changes in the absorption perturbation affect the SSNRs, we select the readings of just one representative detector (in this case detector 3) to limit the amount of data shown in one graph. In the reference case (just described in section 3.1) the absorption coefficient of the perturbation is twice as high as the absorption coefficient of the background medium. Now we add cases in which the absorption coefficient inside the heterogeneity is 1.5 and 1.2 times higher than in the background medium. Figures 3(a) and 3(b) graph the $SSNR_{AC}$ and $SSNR_{\phi}$, respectively. One can observe in the $SSNR_{AC}$ and $SSNR_{\phi}$ plots that as the absorption inside the heterogeneity is increased, the SSNR values increase. However, while the $SSNR_{AC}$, decreases monotonically as the source-modulation is increased, the $SSNR_{\phi}$ plots show a distinct maximum at 400MHz.

3.1.2. Absorption perturbation size

Next, we examine how changes in the size of a heterogeneity influence the SSNRs on the detectors. Cylindrical perturbations with radius of 0.15cm, 0.25cm (reference case), and 0.35cm were tested. Results for these cases are

*Here μ_a and μ_s are absorption and scattering coefficient and OO' is the offset of perturbation center from the homogenous background center. For all the cases the background optical properties are set with $\mu_a = 0.05cm^{-1}$, $\mu_s = 10.0cm^{-1}$, and $g=0.7$.

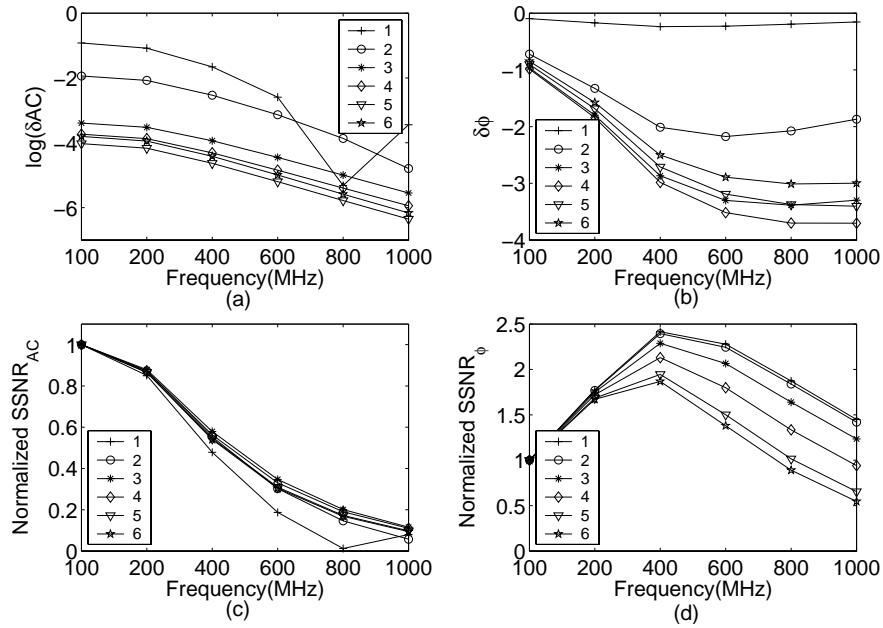


Figure 2. Signal's amplitude sensitivity (δAC) (a) and phase sensitivity ($\delta\phi$) (b) of the reference case listed in Table 1 and their $SSNR_{AC}$ (c) and $SSNR_{\phi}$ (d). Here, 1 to 6 refer to the detectors arranged around the boundary, 1 being the closest detector to the source and 6 the farthest from the source (see also Fig. 1).

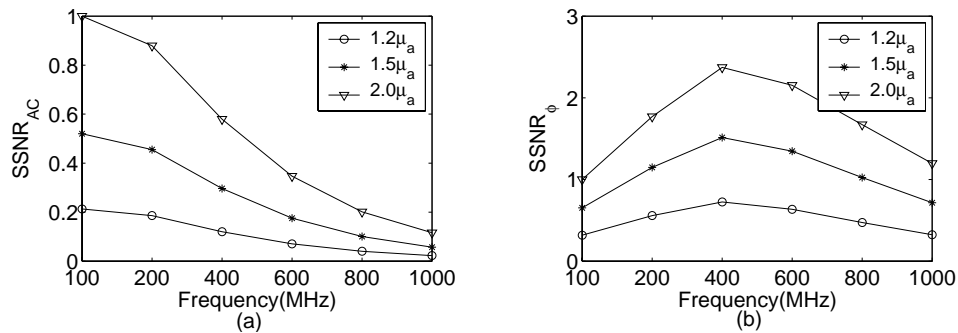


Figure 3. $SSNR_{AC}$ (a) and $SSNR_{\phi}$ (b) with varied strength of absorption perturbation, $1.2\mu_a$, $1.5\mu_a$, $2.0\mu_a$.

shown in Figures 4(a) and 4(b). As expected, we observe that with increasing perturbation size the $SSNR_{AC}$ and $SSNR_{\phi}$ increase. Again the $SSNR_{AC}$ monotonically decreases with modulation frequency with all perturbation size, while the $SSNR_{\phi}$ shows a maximum at $\sim 400\text{MHz}$.

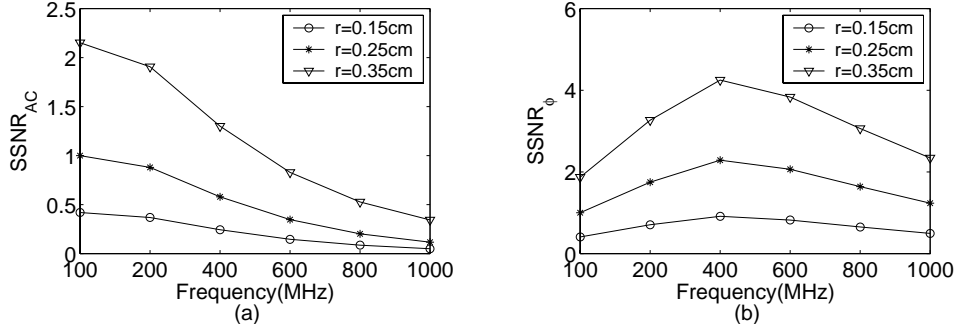


Figure 4. $SSNR_{AC}$ (a) and $SSNR_{\phi}$ (b) with varied size of absorption perturbation, $r = 0.15\text{cm}$, 0.25cm , 0.35cm .

3.1.3. Absorption perturbation location

Here, we examine how perturbation location affects the system's detection limitation. The center of perturbation (O') was placed in different locations ($OO' = 0.0\text{ cm}$, 0.25 cm (reference case) and 0.5 cm) on the line OS in Fig. 1. The perturbation strength ($2.0\mu_a$) and size ($r = 2.5\text{ mm}$) were fixed, while the source modulation frequencies varied from 100 to 1000 MHz. Results are shown in Figures 5(a) and 5(b). The $SSNR_{AC}$ monotonically decreases with modulation frequency at different OO' and the $SSNR_{\phi}$ shows a maximum value at 200–400 MHz depending on the position of perturbation center. These two graphs also reveal that when the heterogeneity gets closer to the source the SSNR values become increasingly bigger. Therefore, it is easier to detect the presence of the heterogeneity in these cases.

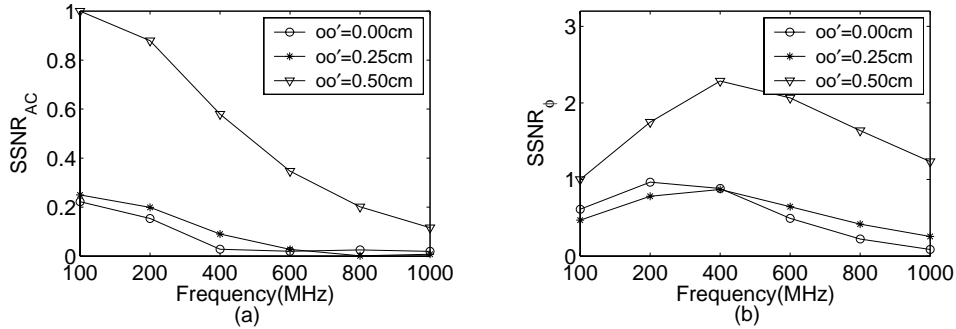


Figure 5. $SSNR_{AC}$ (a) and $SSNR_{\phi}$ (b) by moving the location of absorption perturbation, $OO' = 0.0\text{cm}$, 0.25cm , 0.50cm .

3.2. SSNR studies with scattering perturbations

Physically, light absorption is a phenomenon in which photons are eliminated, while light scattering is a phenomenon in which the trajectories of the photons are changed. Thus, changing a tissue's absorption properties decreases (or increases) the amount of photons arriving at the detectors, while changing a tissue's scattering properties will redistribute the number of photons that arrive at the different detectors.

In this section, we examine cases where the scattering properties of the heterogeneity vary, while the absorption properties of the heterogeneity are constant and identical to that of the background medium. A summary of all cases used in the numerical experiments can be found in Table 2.

Table 2. Summary of different cases used for the sensitivity analysis with scattering perturbations

	Testing Cases [†]	$\mu_a(cm^{-1})$	$\mu_s(cm^{-1})$	r (cm)	OO'(cm)
	reference case				
	$2.0\mu_s, r = 0.25cm, OO' = 0.50cm$	0.05	20.0	0.25	0.5
Strength	$1.2\mu_s$	0.05	12.0	0.25	0.5
	$1.5\mu_s$	0.05	15.0	0.25	0.5
Size	$r = 0.15cm$	0.05	20.0	0.15	0.5
	$r = 0.35cm$	0.05	20.0	0.35	0.5
Location	$OO' = 0.0cm$	0.05	20.0	0.25	0.0
	$OO' = 0.25cm$	0.05	20.0	0.25	0.25

As in the study of the absorption perturbation, the reference case was analyzed first. Investigating the δAC and $\delta\phi$ with scattering perturbation shown in Figures 6(a) and 6(b), we find the signal's sensitivities trend to be different from those caused by the absorption perturbation. The δAC s are almost independent of the modulation frequency at the detectors close to the source (Fig. 7a, detectors 1 and 2). For the detectors further away from the source, more complex frequency-dependences are observed, as some detectors (3 and 4) monotonically increase, while others take on a minimum values between 200 - 400 MHz (detectors 5 and 6). In general, the $\delta\phi$ s increase with the modulation frequency, except for detector 2.

Figures 6(c) and 6(d) show $SSNR_{AC}$ and $SSNR_{\phi}$, respectively. In most cases the $SSNR_{AC}$ curves show maximums for source-modulation frequencies between 400 and 600 MHz. However, $SSNR_{AC}$ curves for detectors 5 and 6, both far away from the source, have some minimum value at 200 and 400MHz respectively. $SSNR_{\phi}$ curves all show a maximum value at 400 MHz, except the curve for detector 1, which strongly increases after it takes on a minimum value at 200 MHz.

3.2.1. Scattering perturbation strength

In Figures 7(a) and 7(b), $SSNR_{AC}$ s and $SSNR_{\phi}$ s are plotted for the case when the scattering coefficients in the heterogeneity varies from $1.0 cm^{-1}$ to $2.0 cm^{-1}$ corresponding to the contrast ratio between 1.2 to 2.0. Similar to the case of the absorption perturbation, we observe that SSNRs increase with the strength of perturbation. However, the $SSNR_{AC}$ s with scattering perturbation show maximum values at around 600 MHz, while in the absorption perturbation cases the $SSNR_{AC}$ monotonically decreased with increasing modulation frequency. The $SSNR_{\phi}$ curves again reach maximum values at 400MHz.

3.2.2. Scattering perturbation size

The impacts of size of scattering perturbations are plotted in Figures 8(a) and 8(b). From these plots, we find that $SSNR_{\phi}$ s improve with the enlargement of the perturbation size. Compared to previous cases, all $SSNR_{\phi}$ s keep their peak values at 400MHz. On the other hand the position of the maximum in the $SSNR_{AC}$ curves moves from 600 MHz to 800MHz.

3.2.3. Scattering perturbation location

Changing the position of the perturbation leads to a shift of the maximum in the $SSNR_{AC}$ and $SSNR_{\phi}$ curves (see Fig. 10). As mentioned before, scattering is a procedure of redistribution of photons; thus, the location of the perturbation effect the different detector's signal sensitivity. In Fig.9(a), the centrally located perturbation reaches its maximum $SSNR_{AC}$ at the low modulation frequency, while in the cases of off-center perturbation, the maximum $SSNR_{AC}$ value reached at higher frequency. The $SSNR_{\phi}$ is more complicated. Fig.9(b) shows that deep embedded perturbation has a much lower SSNR compared with that near the surface, which means it is hard to detect and characterize the centrally located perturbations.

[†]Here μ_a and μ_s are absorption and scattering coefficient and OO' is the offset of perturbation center from the homogenous background center. For all the cases the background optical properties are set with $\mu_a = 0.05cm^{-1}$, $\mu_s = 10.0cm^{-1}$, and $g=0.7$.

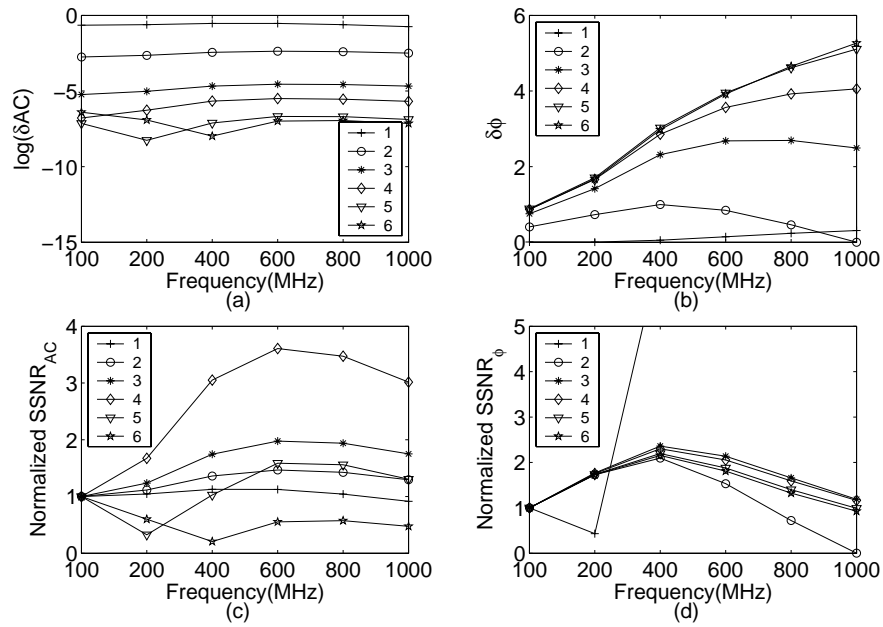


Figure 6. Signal's amplitude sensitivity (δAC) (a) and phase sensitivity ($\delta\phi$) (b) of the reference case listed in Table 2 and their $SSNR_{AC}$ (c) and $SSNR_{\phi}$ (d). Here, 1 to 6 refer to the detectors arranged around the boundary, 1 being the closest detector to the source and 6 is the farthest from the source (see also Fig. 1).

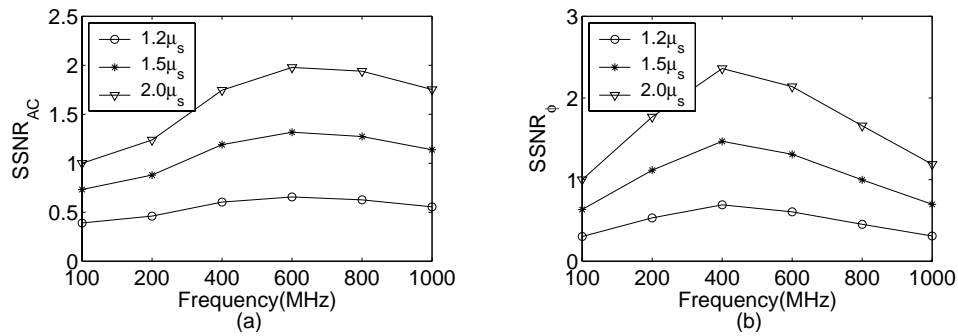


Figure 7. $SSNR_{AC}$ (a) and $SSNR_{\phi}$ (b) with varied strength of scattering perturbation, $1.2\mu_s$, $1.5\mu_s$, $2.0\mu_s$.

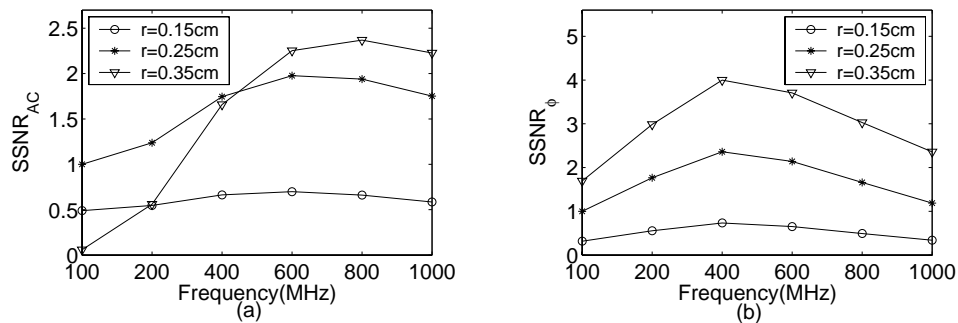


Figure 8. $SSNR_{AC}$ (a) and $SSNR_{\phi}$ (b) with varied size of scattering perturbation, $r = 0.15\text{cm}$, 0.25cm , 0.35cm .

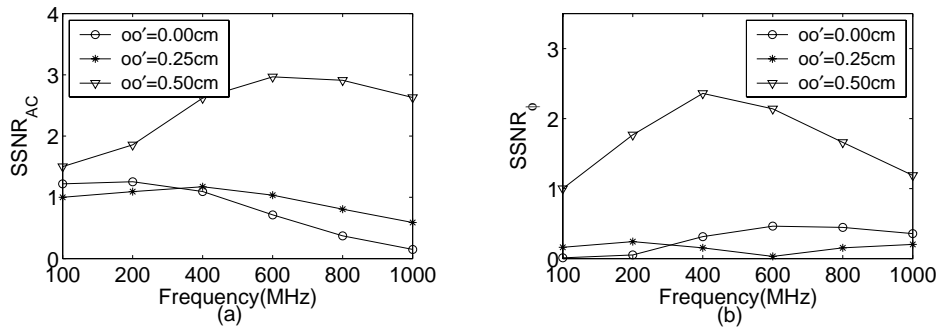


Figure 9. $SSNR_{AC}$ (a) and $SSNR_{\phi}$ (b) by moving the location of scattering perturbation, $OO' = 0.0\text{cm}$, 0.25cm , 0.50cm .

4. DISCUSSION AND CONCLUSIONS

This work focused on the sensitivity analysis concerning the effects of optical heterogeneities in a cylindrical volume, which mimics small geometries often encountered in optical tomographic imaging of small animals or human fingers. The analysis was based on solutions to the frequency-domain equation of radiative transfer, which provides more accurate results than the widely employed diffusion approximation. Using different source modulation frequencies, we studied the effects of size, location, strength, and optical properties on the detectability of embedded heterogeneities.

We found that in general, one can distinguish four different situations: two for the case of an absorbing heterogeneity and two for the case of a scattering heterogeneity. If the heterogeneity is purely absorbing, the $SSNR_{AC}$ is always largest for a modulation frequency of 0 Hz. This result is not surprising and in agreement with previous works by other groups^{9,10}. However, the $SSNR_{\phi}$ shows in this case consistently an optimal value for source modulation frequencies around 400 MHz. While the phase delay is monotonously increasing with increasing modulation frequency, this does not automatically lead to more and more accurate phase measurements; the noise (defined as standard deviation) in the phase measurements is also increasing with increasing modulation frequency. Combining these two effects results in an optimal modulation frequency for which the $SSNR_{\phi}$ is largest. When scattering heterogeneities are considered a more complex picture occurs. Now even the $SSNR_{AC}$ shows optimal values at non-zero modulations frequencies. While the $SSNR_{\phi}$ is again the largest for modulation frequencies around 400 MHz, for most situations considered in this study, the best $SSNR_{AC}$ is obtained for a variety of values between 200 to 800 MHz, depending in the size and location of the heterogeneity inside the medium. These findings suggest that frequency-domain optical tomographic imaging system for small animal studies should focus on source modulation frequency below 800 MHz. If only one frequency is to be used, 400 MHz appears optimal. However, a multi-frequency system that allows to perform amplitude measurements at various frequencies ranging from 0 to 800 MHz, and phase measurements between 300 and 500 MHz promises to capture most type of effects.

Acknowledgement

We would like to thank James Masciotti and Uwe Netz for many useful discussion and helpful suggestion concerning this manuscript. This work was supported in part by the National Institute of Arthritis and Musculoskeletal and Skin Diseases (NIAMS-2R01-AR046255) and the National Institute of Biomedical Imaging and Bioengineering (NIBIB-R01EB001900), which are both divisions of the National Institutes of Health (NIH).

REFERENCES

1. O. Dorn, "A transport-backtransport method for optical tomography," *Inverse Problems* **14**(5), pp. 1107–1130, 1998.
2. A. D. Klose and A. H. Hielscher, "Iterative reconstruction scheme for optical tomography based on the equation of radiative transfer," *Med. Phys.* **26**, pp. 1698–1707, 1999.

3. A. D. Klose, U. Netz, J. Beuthan, and A. H. Hielscher, "Optical tomography using the time-independent equation of radiative transfer. part 1: Forward model," *J. Quant. Spectrosc. Radiat. Transfer* **72**, pp. 691–713, 2002.
4. A. D. Klose and A. H. Hielscher, "Optical tomography using the time-independent equation of radiative transfer. part 2: Inverse model," *J. Quant. Spectrosc. Radiat. Transfer* **72**, pp. 715–732, 2002.
5. A. D. Klose and A. H. Hielscher, "Quasi-newton methods in optical tomographic image reconstruction," *Inverse Problems* **19**, pp. 387–409, 2003.
6. G. Abdoulaev and A. H. Hielscher, "Three-dimensional optical tomography with the equation of radiative transfer," *Journal of Electronic Imaging* **12**(4), pp. 594–560, 2003.
7. K. Ren, G. S. Abdoulaev, G. Bal, and A. H. Hielscher, "Algorithm for solving the equation of radiative transfer in the frequency domain," *Opt. Lett.* **29**(6), pp. 578–580, 2004.
8. K. Ren, G. S. Abdoulaev, G. Bal, and A. H. Hielscher, "Frequency-domain optical tomography with the equation of radiative transfer," *SIAM Journal on Scientific Computing(SISC)* **28**(4), pp. 1463–1489, 2006.
9. D. A. Boas, M. A. O'Leary, B. Chance, and A. G. Yodh, "Detection and characterization of optical inhomogeneities with diffuse photon density waves: a signal-to-noise analysis," *Appl. Opt.* **36**(1), pp. 75–92, 1997.
10. V. Toronov, E. D'Amico, D. Hueber, E. Gratton, B. Barbieri, and A. Webb, "Optimization of the signal-to-noise ratio of frequency-domain instrument for near-infrared spectro-imaging of the human brain," *Opt. Expr.* **11**(21), pp. 2117–2729, 2003.
11. F. Fedele, J. P. Laible, and M. J. Eppstein, "Coupled complex adjoint sensitivities for frequency-domain fluorescence tomography: Theory and vectorized implementation," *J. Comput. Phys.* **187**, pp. 597–619, 2003.
12. L. Henyey and J. Greenstein, "diffuse radiation in the galaxy," *Astrophys. J.* **90**(16), pp. 70–83, 1941.
13. A. Welch and M. Van-Gemert, *Optical-thermal Response of Laser Irradiated Tissues*, Plenum Press, New York, 1995.
14. S. Arridge and W. Lionheart, "Nonuniqueness in diffusion-based optical tomography," *Opt. Lett.* **23**(11), pp. 882–884, 1998.
15. T. Tao, Y. Chen, J. Zhang, X. Intes, and B. Chance, "Analysis on performance and optimization of frequency-domain near-infrared instruments," *J. BioMed. Opt.* **7**(4), pp. 643–649, 2002.
16. X. Gu, K. Ren, and A. Hielscher, "Frequency-domain sensitivity analysis for small imaging domains using the equation of radiative transfer," *Appl. Opt.* **46**(10), pp. 1624–1632, 2007.